Accumulation of Deep Traps at Grain Boundaries in Halide Perovskites

Ji-Sang Park,*,† Joaquín Calbo,† Young-Kwang Jung,‡ Lucy Whalley,† and Aron Walsh*,†,‡

†*Department of Materials, Imperial College London, Exhibition Road, London SW7 2AZ, UK*

‡*Department of Materials Science and Engineering, Yonsei University, Seoul 03722, Korea*

E-mail: ji-sang.park@imperial.ac.uk; a.walsh@imperial.ac.uk

Abstract

The behaviour of grain boundaries in polycrystalline halide perovskite solar cells remains poorly understood. Whereas theoretical studies indicate that grain boundaries are not active for electron-hole recombination, there have been observations of higher non-radiative recombination rates involving these extended defects. We find that iodine interstitial defects, which have been established as a recombination center in bulk crystals, tend to segregate at planar defects in $CsPbI_3$. First-principles calculations show that enhanced structural relaxation of the defects at grain boundaries results in increased stability (higher concentration) and deeper trap states (faster recombination). We show how the grain boundary can be partly passivated by halide mixing or extrinsic doping, which replaces or suppresses the formation of trap states close to the grain boundaries.

Hybrid inorganic-organic perovskite solar cells have attracted much attention because of their superior material properties,[1–5] inexpensive fabrication methods,[6,7] and rapidly in-

creasing solar conversion efficiency. An intrinsic defect tolerance[8–11] has contributed to the rapid optimization of halide perovskite solar cells from 3.8%[12] to more than 24% within 10 years.[13,14] For further development, a deeper understanding of defect properties is needed to tune the Fermi level and suppress carrier recombination.[14,15] The absorber layer in halide perovskite solar cells is usually grown in polycrystalline forms,[3,16] and thus not only the bulk properties but also the interfacial properties between the grains should be considered.[17–19]

Whether extended defects such as grain boundaries are beneficial or detrimental to device performance is still under active debate.[2,16,20–27] On one hand, Kelvin probe force microscopy and conductive atomic force microscopy measurements have shown that charges are efficiently separated and collected at grain boundaries in $CH_3NH_3PbI_3$.[21] In contrast, confocal fluorescence microscopy measurements correlated with scanning electron microscope measurements report that the photoluminescence (PL) intensity is lower in grain boundaries, and that this can be attributed to faster non-radiative recombination.[22] Weak PL intensity does not necessarily indicate shorter lifetimes and higher recombination,[27] whereas grain boundaries can still interfere with charge transport properties.[28] Several passivation strategies have been proposed, for example, using excess methylammonium iodide (MAI),[23] methylammonium bromide (MABr),[29] phenethylammonium,[30] and potassium iodide,[17] based on the argument that grain boundaries are strong recombination centers.

Different conclusions can also be found in computational investigations. Several density functional theory (DFT) studies have claimed that grain boundaries do not introduce deep gap states.[20,26,31] On the other hand, an explanation of the more rapid carrier recombination at grain boundaries in $CH_3NH_3PbI_3$ was made based on the reduced bandgap by excited-state molecular dynamics simulations.[24] It was also claimed that the $\Sigma 3$ [120] grain boundaries in $CsPbBr_3$ act as electron barriers and hole sinks.[31] For the mixed halide perovskites, McKenna reported iodine enrichment at grain boundaries,[32] resulting in a reduced bandgap that implies faster electron-hole recombination will take place.

Although well-ordered (pristine) grain boundaries are usually used as model systems in

DFT calculations,[20,24,26,32] the actual grain boundaries can be non-stoichiometric and disordered. Grain boundaries usually serve as reservoirs for defect segregation.[33–35] Experimental studies show that the I^- ions in halide perovskites can easily migrate through the bulk[36] and across grain boundaries.[34,37] This agrees with DFT calculations that predict low migration barriers and high mobilities for the iodine interstitals.[38] Since defect electronic structure depends on the local atomic structure of the grain boundary,[33,35,39] the stability of point defects at, or near, grain boundaries should be thoroughly examined to determine whether grain boundaries are detrimental or beneficial to device performance.

In this Letter, we show that the grain boundaries in halide perovskites can attract point defects and facilitate the formation of deeper trap levels. By performing first-principles DFT calculations on $CsPbI_3$ as a model system, we found that iodine interstitials in both the positive charge state (I_i^+) and negative charge state (I_i^-) are energetically more stable at the grain boundary than in the bulk. Since both defect charge states introduce sub-bandgap levels that can act as recombination centers, grain boundaries with a high concentration of the defects become carrier traps. Enhanced stability of the interstitial defects at grain boundaries is explained in terms of structural relaxation, which alters the electrical properties of defects accordingly. We also found that I_i^- defects at the grain boundary can be partially replaced by the negatively charged Br interstitial (Br_i^-). Br_i^- introduces shallower levels at the grain boundary and so we expect this process to reduce the rate of non-radiative recombination.

Grain boundary model. The polymorphs of $CsPbI_3$ and an atomistic model of the grain boundary are shown in Figure 1. We chose the $\Sigma5$ [130] grain boundary because of its low formation energy.[26] We initially attempted to construct atomistic models from the cubic and tetragonal polymorphs but found that there were spontaneous transitions to the orthorhombic phase when an iodine interstitial was incorporated in the grain interior. However, the defects at the grain boundary do not always promote a phase transition, leading to unreliable segregation energies. We circumvent this problem by including orthorhombic rotations in

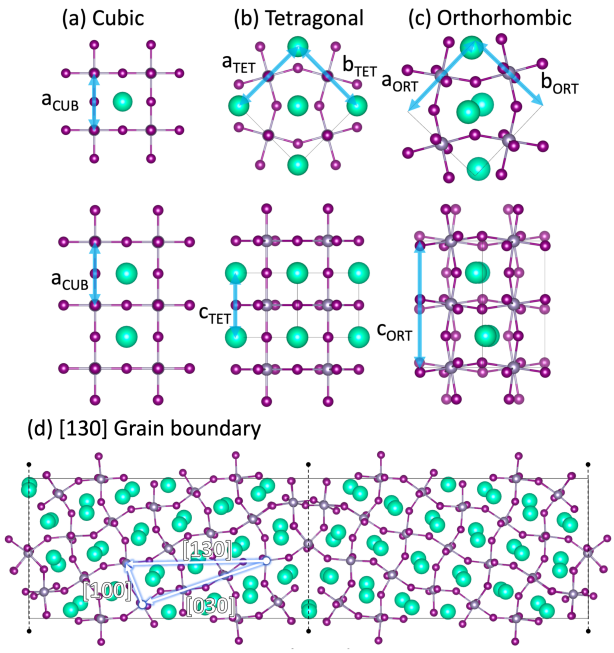

Figure 1: (a,b,c) Atomic structure of three polymorphs of $CsPbI_3$ (top and side views are displayed). (d) atomic model of the $\Sigma 5$ [130] symmetric tilt grain boundary. The solid lines show the boundary of the cells, and the dashed lines represent the grain boundaries. The lattice constants are denoted as a, b, c.

our grain boundary models, under the lattice vector constraint that $a = b \neq c$ to faciliate the model construction. Since our stoichiometric grain boundary model contains both fully coordinated PbI_6 and under-coordinated PbI_5, we are able to analyze the stability of defects in various environments. The formation energy of the grain boundary with respect to orthorhombic $CsPbI_3$ is 1.45 eV/nm^2 (0.23 J/m^2). This is more stable than typical grain boundary energies in Si and CdTe.[33,40] Our pristine grain boundary model does not introduce any electronic states deep in the bandgap (see Figure S1), consistent with previous studies.[20,26,31]

Iodine interstitials. It is well established that the iodine interstitial is a mobile species in the perovskite crystal.[34,36,37,41] Since the migration barrier energy of an I interstitial is small,[38] it should be easy for the iodine interstitials to accumulate at a grain boundary if this is the energetically favourable defect site. Meggiolaro *et al.* has shown that excess iodine in the form of I_i^- defects is stable on (001) surfaces of $CH_3NH_3PbI_3$.[42] Furthermore,

DFT calculations including Hartree-Fock exchange and spin-orbit coupling show that this defect introduces thermodynamic transition levels in the bandgap.[43,44] Thind *et al.* reported that Br vacancies at the $\Sigma5$ [120] grain boundary introduce deep levels in $CH_3NH_3PbBr_3$.[31] However, we do not consider the halide vacancy in this study because of its shallow nature in $CH_3NH_3PbI_3$.[43–45] The $CH_3NH_3^+$ interstitial has been predicted to have relatively low migration barrier,[38] but there are experimental studies reporting its slow diffusivity.[36,46] We do not consider it here as it does not introduce electronic states in the bandgap.[44]

The atomic structure of I_i strongly depends on its charge state.[43,44,47] I_i^- forms the split interstitial H-center as shown in Figure 2a.[47] I_i^+ forms a I−I−I trimer by bridging two opposite lattice iodine as shown in Figure 2c, a configuration that is also found in other perovskite-derived materials.[48] Note that the neutral iodine interstitial is predicted to be thermodynamically unstable at all Fermi levels, and thus it is not considered in the simulations.[43,44] Based on this knowledge, we placed iodine interstitials in either the negative or positive charge state at sites in the grain boundary model to investigate segregation behavior. To avoid bias, we constructed a three-dimensional grid spanning 1 nm across the grain boundary, and placed an interstitial defect at each point. Only the grain boundary models with a minimum interstitial-lattice ion distance longer than 2.5 Å were chosen, as this length is shorter than the bond lengths of Pb−I and I−I.

Stability of iodine interstitials. The relative energy of I_i defects with respect to that in the bulk-like region are summarized in Fig. 2d and 2e. We find that I_i^- forms a split interstitial, while I_i^+ forms a trimer when positioned far from the grain boundary (>5 Å). At the grain boundary, the interstitial defects take various configurations and have widely varying formation energies. The I_i^- defect can form bonds with one or two under-coordinated Pb atoms, which is the most favoured configuration at the grain boundary (Figure 2b). I_i^- can be also located in a void region, where there is no preferential binding to a specific atom. This is less stable than the other configurations. For the 1− and 1+ charge states, the stable configuration has a respective formation energy 0.57 eV and 0.49 eV lower than in the

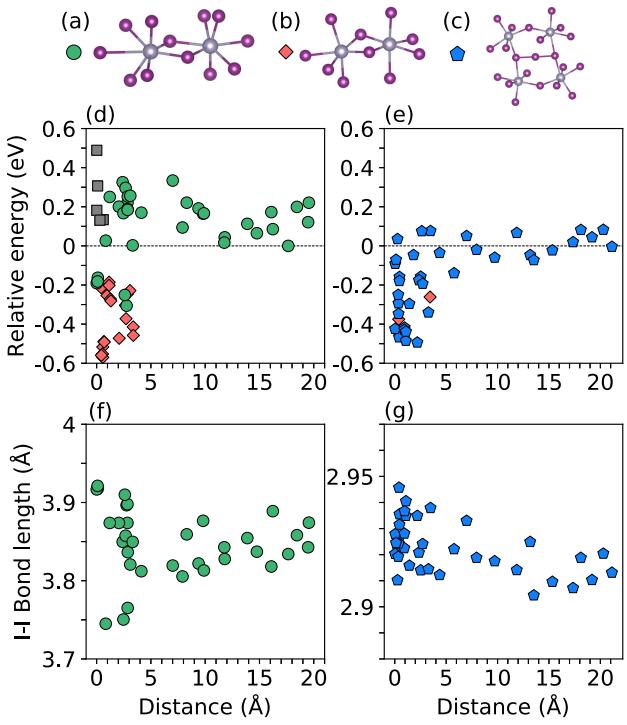

Figure 2: Defect profiles as a function of distance from the grain boundary in $CsPbI_3$. (a) A split interstitial (I–I) denoted by a green circle. (b) A red diamond represents an interstitial forming Pb–I bonds with under-coordinated Pb atoms. (c) A blue pentagon represent an iodine trimer (I–I–I). A grey square represents an interstitial in a void region. The relative formation energy of (d) negatively charged (I_i^-) and (e) positively charged (I_i^+) iodine interstitial defects. The formation energy of the structure with the lowest energy in the bulk-like region is set to 0 eV. Bonding distance between I atoms in (f) I_i^- and (g) I_i^+ defects.

bulk region. If we exclude the defects that passivate the under-coordinated Pb atoms, the segregation energy of I_i^-, which is the energy gain by accumulation at the grain boundary, is 0.31 eV. As will be discussed in the below, the stabilization of the grain boundary defects are largely correlated with their local structure.

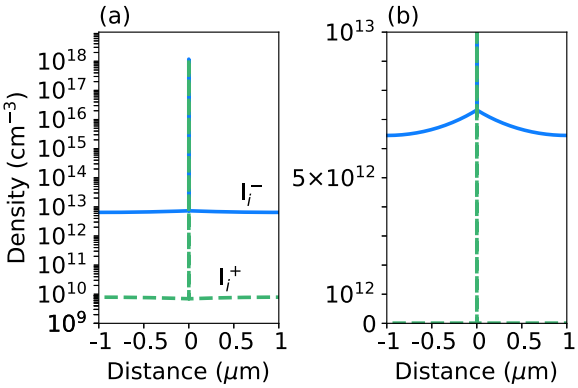

Figure 3: Calculated density of iodine interstitial defects around a grain boundary in $CsPbI_3$ obtained as a solution to Poisson's equation for a system of charged interstitials and free carriers. Note that the y-axis is logarithmic in (a) and linear in (b).

To investigate the impact of the large segregation energy on the defect profiles, we obtained the Fermi level and density of defects near grain boundaries by solving Poisson's equation in one-dimension, as shown in Figure 3. The potential ϕ and the charge density ρ satisfy

$$\nabla^2\phi = -\frac{\rho}{\epsilon}, \tag{1}$$

where ϵ is the dielectric constant. The charge density is calculated by summing the charge carriers and ionized defects, which are determined by the Fermi level. Iodine interstitial defects and free carriers were considered in the calculation assuming an iodine rich growth condition. Detail of the implementation is explained in the calculation methods section.

Due to the large segregation energy, the defect density at grain boundary can be as high as 10^{18} cm^{-3} ($\sim 10^{11}$ cm^{-2}), as shown in Figure 3a. The Fermi level at the grain boundary is pinned at 0.58 eV higher than the valence band edge. This energy is 0.09 eV higher than the $\epsilon(1/-1)$ thermodynamic transition level of the I_i defect in bulk $CsPbI_3$

(0.49 eV), as the segregation energy of I_i^+ defect is 0.18 eV higher than the segregation energy of I_i^- defect. The excess amount of I_i^+ at the grain boundaries is compensated by the larger concentration of I_i^- in grain interiors in the simulation. We also find that I_i^- defects are weakly accumulated near grain boundaries (see Figure 3b), whereas the band is not significantly bent because of the low concentration. We conclude that both charge states of the iodine interstitial segregate at grain boundaries, and therefore the local concentration of point defects in polycrystalline halide perovskite materials is higher than that would be expected from a bulk defect calculation.

Electronic structure of I_i defects. As in the bulk perovskite, the I_i^+ and I_i^- defects at boundaries introduce transition levels in the bandgap. Previous studies indicate that the average bond length is related to the electronic properties of the iodine interstitial. Whalley *et al.* have shown that optical excitation energies of halide dimers generally decrease as the dimer bond length increases.[47] Meggiolaro *et al.* also found that the formation energy of the defects largely change with the bond lengths.[44] In our calculations, the I_i^- defect bonds with a neighbouring lattice iodine with a bond length of 3.83 Å in the bulk-like region. This bond length ranges from 3.75 Å up to 3.92 Å at the grain boundary, as shown in Figure 2c. The I_i^+ defect bonds in a I−I−I trimer with an average bond length of 2.91 Å in the bulk-like region. The average bond length of the iodine trimer is increased when the defect is located at the grain boundary ($\leq$2.95 Å) as depicted in Figure 2d. We conclude that the iodine interstitial defects are stabilized at the grain boundary as the iodine bonds are less strained by neighboring atoms (see Figure S2).

We employ a molecule-in-crystal approach with dielectric embedding[49] to calculate the defect levels at the grain boundaries (see calculation methods). Interstitial defects like I_i^- and I_i^+, which form a dimer and a trimer, were modeled as ${I_2}^{2-}$ and ${I_3}^-$, respectively. The ideal bond length of an embedded I_3 trimer is 3.05 Å, longer than the longest bond length found in the grain boundary calculation (2.95 Å). However, geometry optimization of the embedded dimer I_2^{2-} leads to its dissociation, indicating that the neighboring Pb atoms in

the crystal are needed to maintain the bonding. The acceptor level and the donor level of I_i^- and I_i^+, which are estimated using ionization potential (IP) and the electron affinity (EA), respectively, are summarized in Figure 4. The acceptor level of I_i^- is related to hole trapping, whereas the donor level of I_i^+ corresponds to electron trapping. The charge transition levels of I_i defects in bulk $CsPbI_3$ obtained from hybrid DFT calculations (HSE06) with spin-orbit coupling were used as reference.

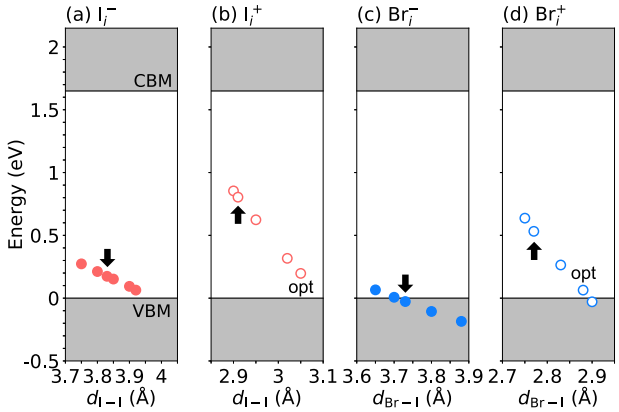

Figure 4: Charge transition levels of (a) I_i^-, (b) I_i^+, (c) Br_i^-, and (d) Br_i^+. The valence band maximum (VBM) and the conduction band minimum (CBM) were denoted as horizontal lines. The optimized bond length for the embedded molecule is denoted as opt. The levels calculated using the bond length found in the bulk-like region are denoted by black arrows.

We find that I_i^- and I_i^+ defects introduce acceptor and donor levels in the bandgap, respectively, and that their levels are correlated with bond length (Figure 4). As the average bond length is increased at the grain boundary, the donor level lowers in energy, leading to deeper states with respect to the conduction band edge. Since each I_i^+ defect introduces levels for electron capture, we expect that segregation of I_i^+ defects at the grain boundary should reduce the electron carrier lifetime. I_i^- introduces the acceptor level slightly above the valence band edge in the grain interior. For the majority of I_i^- defects located near the grain boundary, the I–I bond is lengthened (Figure 2c) and the energy of the acceptor level is lowered. This will promote the de-trapping of hole carriers, and make I_i^- defects at grain boundaries less detrimental than those in the grain interior. However this benefit is counterbalanced by the high concentration of defects.

Suppress trapping by halide mixing. We have demonstrated that defect segregation at the grain boundary will lead to defect properties that are detrimental to device performance. We now investigate possible mitigation strategies. One option is to incorporate other chemical elements to substitute the atoms that contribute to the gap states at grain boundaries. This has been investigated in the context of the photovoltaic material CdTe, where passivation by heterovalent alloying was shown to be effective.[50] In CdTe solar cells, S atoms segregate at grain boundaries and replace Te−Te anti-bonding levels, which introduce deep level in the gap, by shallower S−Te or S−S levels. The beneficial role of S substitution for Te is attributed to lower p-orbital levels and weaker interaction between the orbitals. A similar approach can be applied to halide perovskites as the halide *p*-*p* anti-bonding states form interstitial defect levels, and Br and Cl have lower *p* orbital levels than iodine. Effect of Cl substitution has been examined in a previous study.[20]

To examine whether the accumulation of I_i at grain boundary can be suppressed by Br_i, we calculate the energy required to exchange an I_i defect and a Br atom at a lattice site ($I_i + Br_I \rightarrow I_I + Br_i$). We find that an energy of 0.44 eV and -0.04 eV is needed to form Br_i^+ and Br_i^- in the bulk region, respectively. Thus, if there is an I_i^- in the bulk region, then it is energetically favourable to swap with a Br atom, to produce a Br_i^- defect. However, an I_i^+ interstitial will not spontaneously exchange to form Br_i^+, in good accord with a previous study of Meggiolaro *et al.* in $CH_3NH_3PbI_3$.[44]

We have further considered the segregation energy of Br interstitials in $CsPbI_3$. We find that both Br_i^- and Br_i^+ segregate to the grain boundary as shown in Figure 5a and 5b, respectively. Br_i^- prefers to make bonds with under-coordinated Pb atoms and have a segregation energy of 0.52 eV, slightly smaller than that calculated for I_i^-. If we compare the defects forming split interstitials, then a segregation energy of 0.23 eV is obtained. Based on the smaller segregation energies and slightly favored formation of Br_i^- in grain interior, we expect that both Br_i^- and I_i^- are likely formed at grain boundaries. In contrast to I_i^+, the Br_i^+ defect has a stronger preference to bond with under-coordinated Pb atoms, resulting in

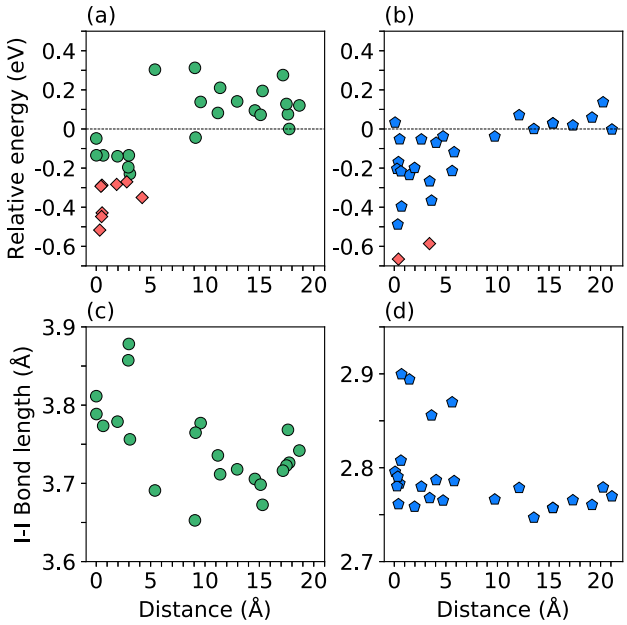

Figure 5: The relative formation energy of (a) negative charged (Br_i^-) and (b) positively charged (Br_i^+) bromine interstitial defects as a function of distance from the grain boundary in $CsPbI_3$. The average Br-I distance forming (c) Br_i^- and (d) Br_i^+ defects. Green circle represents a split interstitial (Br−I); red diamond represents a Br interstitial bonding with under-coordinated Pb atoms (Br−Pb); blue pentagon represents trimer formation (I−Br−I).

a segregation energy of 0.67 eV, which is larger than that calculated for I_i^+. Otherwise, if we compare the defects that form trimers, then the segregation energy of both Br_i^+ and I_i^+ is close to 0.5 eV. Since I_i^+ is more stable than Br_i^+ in bulk $CsPbI_3$, we predict that Br_i^+ defects are not formed in substantial concentrations at the grain boundary. We therefore conclude that the Br_i^-, I_i^-, and I_i^+ interstitial defects are likely accumulated at the grain boundaries.

The enhanced stability of the Br_i defects at the grain boundary as compared to those in the bulk is also well explained by the increased Br−I bond length (Figure S3). The Br−I bond of Br_i^-, which is 3.73 Å in the bulk region, is lengthened up to 3.88 Å at the grain boundary (Figure 5c). Similarly, the average Br−I bond length of Br_i^+ is 2.77 Å in the bulk region, but can be increased up to 2.90 Å at the grain boundary (Figure 5d).

The formation of Br interstitials will benefit the electronic properties of the material and lower electron-hole recombination compared to an equivalent population of iodine interstitials. As shown in Figure 4, Br_i^- introduces a shallower defect level than the I interstitial.

The formation of Br_i^- at grain boundaries will result in a faster rate of hole de-trapping, following Shockley-Read-Hall statistics, making the grain boundaries less detrimental. However, halide mixing cannot make the boundary completely benign as the formation of I_i^- and I_i^+ defects at the boundaries is likely to occur. Although the presence of Br_i^+ would introduce even deeper levels than I_i^+, we demonstrate that its formation is unfavorable.

Suppress trapping by doping. Extrinsic doping can be used to tune the Fermi level at the grain boundary and suppress the formation of particular charged interstitial defects. For instance, if we increase the Fermi level, then the population of Br_i^- and I_i^- defects could exceed that of I_i^+ as the formation energy of negatively (positively) charged defects decreases (increases). This strategy would reduce recombination at the grain boundary where Br_i^- and I_i^- have shallower levels than their positively charged counterparts. There is evidence that positively charged defects are more detrimental to device performance; a larger capture cross section is reported for the electron trap than that of hole trap in halide perovskites.[51] A recent experimental study by Correa-Baena *et al.* also reported that sample grown under PbI_2-rich conditions, which results in the higher Fermi level,[14] exhibit better photoconversion efficiencies.[52] Otherwise, passivation strategies using halides[17,23,29] might increase the Fermi level at grain boundary by filling iodine vacancies.[53] More comprehensive studies of the recombination properties of defects (e.g. Br_i^-, I_i^-, I_i^+) with consideration of the bond lengthening are however needed to confirm this idea and develop effective passivation strategies.

Intrinsic doping through control of the chemical potentials could produce a similar effect. If halide perovskites are grown under iodine-poor conditions or stoichiometric conditions, then the formation of iodine interstitials is suppressed in grain interiors due to the higher formation energy.[8,44] As a result, reduced defect concentrations at grain boundaries are also expected. The growth mechanism of large-grain polycrystalline perovskites can be also employed to reduce the density of grain boundaries.[3]

In conclusion, we have provided an atomistic explanation for the origin of charge carrier

recombination at grain boundaries in halide perovskites. Taking $CsPbI_3$ as a model system, we found that iodine interstitials segregate to grain boundaries. This confirms that extended defects act as reservoirs for point defects, which can influence dynamic behaviour such as ion transport and current-voltage hysteresis. Interstitial defects at the planar defect form split interstitials (I_i^-), I−I−I trimers (I_i^+), or Pb−I bonds with under-coordinated Pb atoms. When interstitial defects form split interstitial (I−I) or I−I−I trimer, they introduce gap states and promote carrier recombination at the grain boundary. I_i^- at the grain boundary is shown to be less detrimental than that in the grain interior due to an increased bonding length, but this benefit is likely offset by an increased defect concentration. Halide mixing allows I_i^- to be replaced with shallower Br_i^- defects and so can be employed to reduce non-radiative recombination. Defect engineering via controlled growth conditions and Fermi level tuning is discussed as an approach to make the grain boundaries less detrimental.

Calculation methods. An 400 atom model of the Σ5 [130] grain boundary was generated by orienting a perovskite supercell along the [130] direction with lattice parameters $a = 8.606$ Å, $b = 8.606$ Å, $c = 12.695$ Å. The structure model is available from DOI: 10.5281/zenodo.2641358.

To investigate the stability of point defects at near grain boundary, we performed first-principles DFT calculations using a PBEsol exchange-correlation functional[54] and the projector-augmented wave (PAW) method,[55] implemented in the Vienna Ab initio simulation package (`VASP`) code.[56] The plane waves were expanded with cutoff energy of 300 eV. The internal coordinates of the supercell were optimized until the residual forces were below 0.01 eV/Å. The transition levels of I_i in bulk $CsPbI_3$ were obtained using the screened hybrid functional of Heyd, Scuseria, and Ernzerhof (HSE06)[57] with 43% and including spin-orbit coupling. A 1×1×2 Γ-centred k-point grid was used for Brillouin-zone integration.

To estimate the defect concentrations near grain boundaries, we solved Poisson's equation self-consistently by employing a periodic boundary condition. The charge density of defects was obtained from the DFT formation energy of defects. The number of available sites for

defects in grain boundaries was assumed to be same as the grain interior. The band edge density of states was obtained from the calculated effective masses ($m_h = 0.178$, $m_e = 0.155$) and used to calculate the carrier concentration at T = 300 K. We separated narrow grain boundary region and grain interior region, and optimized the potential at the boundaries between the two regions that satisfy the charge neutrality condition of the whole system. The formation energy of I_i^+ and I_i^- when the Fermi level is at the valence band edge was 0.15 eV and 1.13 eV, respectively. The growth temperature was set to 300 K. A simulation using a previously reported formation energy[58] gives a similar result.

To assess the electronic levels of the interstitials as a function of the distance between halide atoms, we treated the halide dimers and trimers embedded in a dielectric medium. The self-consistent reaction field approximation was employed through the polarizable continuum solvent model (PCM)[59,60] with a generic solvent formulation and the dielectric constant of $CsPbI_3$ ($\epsilon = 18.1$)[61] by using the Gaussian-16.A03 suite of programs.[62] Minimum-energy geometries were obtained under the DFT framework using the HSE06 functional[57,63] and the effective-core potential CEP-121G triple-split basis set.[64] Doubly-charged dimers (X_i^-) and singly-charged trimers (X_i^+) were modelled, and their vertical ionization potential and electron affinity, respectively, were calculated. Even in a dielectric medium, doubly-charged dimeric species tend to dissociate; thus, we used single-point calculations at characteristic interatomic distances extracted from the periodic calculations for energy alignment analysis.

Acknowledgement

Via our membership of the UK's HPC Materials Chemistry Consortium, which is funded by EPSRC (EP/L000202), this work used the ARCHER UK National Supercomputing Service (http://www.archer.ac.uk). We are grateful to the UK Materials and Molecular Modelling Hub for computational resources, which is partially funded by EPSRC (EP/P020194/1). This work was supported by supercomputer time awarded through PRACE on the Swiss Na-

tional Supercomputing Center (CSCS) under project pr51. JP thanks the Royal Society for a Shooter Fellowship. JC acknowledges the Generalitat Valenciana for the APOSTD/2017/081 fellowship. LW is funded through the EPSRC (EP/L01551X/1). This work at Yonsei was supported by a National Research Foundation of Korea (NRF) grant funded by the Korean government (MSIT) (No. 2018R1C1B6008728)

References

(1) Brenner, T. M.; Egger, D. A.; Kronik, L.; Hodes, G.; Cahen, D. Hybrid Organicinorganic Perovskites: Low-Cost Semiconductors With Intriguing Charge-Transport Properties. *Nat. Rev. Mater.* **2016**, *1*, 15007.

(2) Huang, J.; Yuan, Y.; Shao, Y.; Yan, Y. Understanding the Physical Properties of Hybrid Perovskites for Photovoltaic Applications. *Nat. Rev. Mater.* **2017**, *2*, 17042.

(3) Kim, D. H.; Park, J.; Li, Z.; Yang, M.; Park, J.-S.; Park, I. J.; Kim, J. Y.; Berry, J. J.; Rumbles, G.; Zhu, K. 300% Enhancement of Carrier Mobility in Uniaxial-Oriented Perovskite Films Formed by Topotactic-Oriented Attachment. *Adv. Mater.* **2017**, *29*, 1606831.

(4) Stranks, S. D. Nonradiative Losses in Metal Halide Perovskites. *ACS Energy Lett.* **2017**, *2*, 1515–1525.

(5) Park, J.-S.; Choi, S.; Yan, Y.; Yang, Y.; Luther, J. M.; Wei, S.-H.; Parilla, P.; Zhu, K. Electronic Structure and Optical Properties of α-CH3NH3PbBr3 Perovskite Single Crystal. *J. Phys. Chem. Lett.* **2015**, *6*, 4304–4308.

(6) Jeon, N. J.; Noh, J. H.; Kim, Y. C.; Yang, W. S.; Ryu, S.; Seok, S. I. Solvent Engineering for High-Performance Inorganic–Organic Hybrid Perovskite Solar Cells. *Nat. Mater.* **2014**, *13*, 897.

(7) Li, X.; Bi, D.; Yi, C.; Décoppet, J.-D.; Luo, J.; Zakeeruddin, S. M.; Hagfeldt, A.; Grätzel, M. A Vacuum Flash–Assisted Solution Process for High-Efficiency Large-Area Perovskite Solar Cells. *Science* **2016**, *353*, 58–62.

(8) Yin, W.-J.; Shi, T.; Yan, Y. Unusual Defect Physics in CH3NH3PbI3 Perovskite Solar Cell Absorber. *Appl. Phys. Lett.* **2014**, *104*, 063903.

(9) Brandt, R. E.; Stevanović, V.; Ginley, D. S.; Buonassisi, T. Identifying Defect-Tolerant Semiconductors With High Minority-Carrier Lifetimes: Beyond Hybrid Lead Halide Perovskites. *MRS Communications* **2015**, *5*, 265–275.

(10) Steirer, K. X.; Schulz, P.; Teeter, G.; Stevanovic, V.; Yang, M.; Zhu, K.; Berry, J. J. Defect Tolerance in Methylammonium Lead Triiodide Perovskite. *ACS Energy Lett.* **2016**, *1*, 360–366.

(11) Park, J. S.; Kim, S.; Xie, Z.; Walsh, A. Point Defect Engineering in Thin-Film Solar Cells. *Nat. Rev. Mater.* **2018**, *3*, 194–210.

(12) Kojima, A.; Teshima, K.; Shirai, Y.; Miyasaka, T. Organometal Halide Perovskites as Visible-Light Sensitizers for Photovoltaic Cells. *J. Am. Chem. Soc.* **2009**, *131*, 6050–6051.

(13) Yang, W. S.; Park, B.-W.; Jung, E. H.; Jeon, N. J.; Kim, Y. C.; Lee, D. U.; Shin, S. S.; Seo, J.; Kim, E. K.; Noh, J. H.; Seok, S. I. Iodide Management in Formamidinium-Lead-Halide–Based Perovskite Layers for Efficient Solar Cells. *Science* **2017**, *356*, 1376–1379.

(14) Cui, P.; Wei, D.; Ji, J.; Huang, H.; Jia, E.; Dou, S.; Wang, T.; Wang, W.; Li, M. Planar P–N Homojunction Perovskite Solar Cells With Efficiency Exceeding 21.3%. *Nature Energy* **2019**, *4*, 150–159.

(15) Park, J.-S.; Walsh, A. Embrace Your Defects. *Nature Energy* **2019**, *4*, 95–96.

(16) Lee, J.-W.; Bae, S.-H.; De Marco, N.; Hsieh, Y.-T.; Dai, Z.; Yang, Y. The Role of Grain Boundaries in Perovskite Solar Cells. *Mater. Today Energy* **2017**, *7*, 149–160.

(17) Abdi-Jalebi, M. et al. Maximizing and Stabilizing Luminescence From Halide Perovskites With Potassium Passivation. *Nature* **2018**, *555*, 497.

(18) Jones, T. W. et al. Lattice Strain Causes Non-Radiative Losses in Halide Perovskites. *Energy Environ. Sci.* **2019**, *12*, 596–606.

(19) Wilson, J. N.; Frost, J. M.; Wallace, S. K.; Walsh, A. Dielectric and Ferroic Properties of Metal Halide Perovskites. *APL Mater.* **2019**, *7*, 010901.

(20) Yin, W.-J.; Chen, H.; Shi, T.; Wei, S.-H.; Yan, Y. Origin of High Electronic Quality in Structurally Disordered CH3NH3PbI3 and the Passivation Effect of Cl and O at Grain Boundaries. *Adv. Electron. Mater.* **2015**, *1*, 1500044.

(21) Yun, J. S.; Ho-Baillie, A.; Huang, S.; Woo, S. H.; Heo, Y.; Seidel, J.; Huang, F.; Cheng, Y.-B.; Green, M. A. Benefit of Grain Boundaries in Organic–Inorganic Halide Planar Perovskite Solar Cells. *J. Phys. Chem. Lett.* **2015**, *6*, 875–880.

(22) deQuilettes, D. W.; Vorpahl, S. M.; Stranks, S. D.; Nagaoka, H.; Eperon, G. E.; Ziffer, M. E.; Snaith, H. J.; Ginger, D. S. Impact of Microstructure on Local Carrier Lifetime in Perovskite Solar Cells. *Science* **2015**, *348*, 683–686.

(23) Son, D.-Y.; Lee, J.-W.; Choi, Y. J.; Jang, I.-H.; Lee, S.; Yoo, P. J.; Shin, H.; Ahn, N.; Choi, M.; Kim, D.; Park, N. G. Self-Formed Grain Boundary Healing Layer for Highly Efficient CH3NH3PbI3 Perovskite Solar Cells. *Nat. Energy* **2016**, *1*, 16081.

(24) Long, R.; Liu, J.; Prezhdo, O. V. Unravelling the Effects of Grain Boundary and Chemical Doping on Electron–Hole Recombination in CH3NH3PbI3 Perovskite by Time-Domain Atomistic Simulation. *J. Am. Chem. Soc.* **2016**, *138*, 3884–3890.

(25) Kim, H. D.; Ohkita, H.; Benten, H.; Ito, S. Photovoltaic Performance of Perovskite Solar Cells With Different Grain Sizes. *Adv. Mater.* **2016**, *28*, 917–922.

(26) Guo, Y.; Wang, Q.; Saidi, W. A. Structural Stabilities and Electronic Properties of High-Angle Grain Boundaries in Perovskite Cesium Lead Halides. *J. Phys. Chem. C* **2017**, *121*, 1715–1722.

(27) Yang, M.; Zeng, Y.; Li, Z.; Kim, D. H.; Jiang, C.-S.; van de Lagemaat, J.; Zhu, K. Do Grain Boundaries Dominate Non-Radiative Recombination in CH3NH3PbI3 Perovskite Thin Films? *Phys. Chem. Chem. Phys.* **2017**, *19*, 5043–5050.

(28) Reid, O. G.; Yang, M.; Kopidakis, N.; Zhu, K.; Rumbles, G. Grain-Size-Limited Mobility in Methylammonium Lead Iodide Perovskite Thin Films. *ACS Energy Lett.* **2016**, *1*, 561–565.

(29) Zhang, T.; Long, M.; Yan, K.; Qin, M.; Lu, X.; Zeng, X.; Cheng, C. M.; Wong, K. S.; Liu, P.; Xie, W.; Xu, J. Crystallinity Preservation and Ion Migration Suppression Through Dual Ion Exchange Strategy for Stable Mixed Perovskite Solar Cells. *Adv. Energy Mater.* **2017**, *7*, 1700118.

(30) Lee, D. S.; Yun, J. S.; Kim, J.; Soufiani, A. M.; Chen, S.; Cho, Y.; Deng, X.; Seidel, J.; Lim, S.; Huang, S.; Ho-Baillie, A. W. Y. Passivation of Grain Boundaries by Phenethylammonium in Formamidinium-Methylammonium Lead Halide Perovskite Solar Cells. *ACS Energy Lett.* **2018**, *3*, 647–654.

(31) Thind, A. S.; Luo, G.; Hachtel, J. A.; Morrell, M. V.; Cho, S. B.; Borisevich, A. Y.; Idrobo, J.; Xing, Y.; Mishra, R. Atomic Structure and Electrical Activity of Grain Boundaries and Ruddlesden-Popper Faults in Cesium Lead Bromide Perovskite. *Adv. Mater.* **2018**, *31*, 1805047.

(32) McKenna, K. P. Electronic Properties of {111} Twin Boundaries in a Mixed-Ion Lead Halide Perovskite Solar Absorber. *ACS Energy Lett.* **2018**, *3*, 2663–2668.

(33) Park, J.-S.; Kang, J.; Yang, J.-H.; Metzger, W.; Wei, S.-H. Stability and Electronic Structure of the Low-Σ Grain Boundaries in CdTe: A Density Functional Study. *New J. Phys.* **2015**, *17*, 013027.

(34) Yun, J. S.; Seidel, J.; Kim, J.; Soufiani, A. M.; Huang, S.; Lau, J.; Jeon, N. J.; Seok, S. I.; Green, M. A.; Ho-Baillie, A. Critical Role of Grain Boundaries for Ion Migration in Formamidinium and Methylammonium Lead Halide Perovskite Solar Cells. *Adv. Energy Mater.* **2016**, *6*, 1600330.

(35) Park, J.-S. Stabilization and Self-Passivation of Symmetrical Grain Boundaries by Mirror Symmetry Breaking. *Phys. Rev. Mater.* **2019**, *3*, 014602.

(36) Senocrate, A.; Moudrakovski, I.; Kim, G. Y.; Yang, T.-Y.; Gregori, G.; Grätzel, M.; Maier, J. The Nature of Ion Conduction in Methylammonium Lead Iodide: A Multimethod Approach. *Angewandte Chemie* **2017**, *129*, 7863–7867.

(37) Shao, Y.; Fang, Y.; Li, T.; Wang, Q.; Dong, Q.; Deng, Y.; Yuan, Y.; Wei, H.; Wang, M.; Gruverman, A.; Shielda, J.; Huang, J. Grain Boundary Dominated Ion Migration in Polycrystalline Organic–Inorganic Halide Perovskite Films. *Energy Environ. Sci.* **2016**, *9*, 1752–1759.

(38) Yang, J.-H.; Yin, W.-J.; Park, J.-S.; Wei, S.-H. Fast Self-Diffusion of Ions in CH3NH3PbI3: The Interstiticaly Mechanism Versus Vacancy-Assisted Mechanism. *J. Mater. Chem. A* **2016**, *4*, 13105–13112.

(39) Liu, C.-Y.; Zhang, Y.-Y.; Hou, Y.-S.; Chen, S.-Y.; Xiang, H.-J.; Gong, X.-G. Self-Passivation Rule and Structure of CdTe Σ3 (112) Grain Boundaries. *Phys. Rev. B* **2016**, *93*, 205426.

(40) Ratanaphan, S.; Yoon, Y.; Rohrer, G. S. The Five Parameter Grain Boundary Character Distribution of Polycrystalline Silicon. *Journal of materials science* **2014**, *49*, 4938–4945.

(41) Walsh, A.; Stranks, S. D. Taking Control of Ion Transport in Halide Perovskite Solar Cells. *ACS Energy Lett.* **2018**, *3*, 1983–1990.

(42) Meggiolaro, D.; Mosconi, E.; De Angelis, F. Formation of Surface Defects Dominates Ion Migration in Lead-Halide Perovskites. *ACS Energy Lett.* **2019**, *4*.

(43) Du, M.-H. Density Functional Calculations of Native Defects in CH3NH3PbI3: Effects of Spin–Orbit Coupling and Self-Interaction Error. *J. Phys. Chem. Lett.* **2015**, *6*, 1461–1466.

(44) Meggiolaro, D.; Motti, S. G.; Mosconi, E.; Barker, A. J.; Ball, J.; Perini, C. A. R.; Deschler, F.; Petrozza, A.; De Angelis, F. Iodine Chemistry Determines the Defect Tolerance of Lead-Halide Perovskites. *Energy Environ. Sci.* **2018**, *11*, 702–713.

(45) Evarestov, R. A.; Senocrate, A.; Kotomin, E. A.; Maier, J. First-Principles Calculations of Iodine-Related Point Defects in CsPbI3. *Phys. Chem. Chem. Phys.* **2019**, *21*, 7841–7846.

(46) Senocrate, A.; Moudrakovski, I.; Acarturk, T.; Merkle, R.; Kim, G. Y.; Starke, U.; Gratzel, M.; Maier, J. Slow CH3NH3+ Diffusion in CH3NH3PbI3 Under Light Measured by Solid-State NMR and Tracer Diffusion. *J. Phys. Chem. C* **2018**, *122*, 21803–21806.

(47) Whalley, L. D.; Crespo-Otero, R.; Walsh, A. H-Center and V-Center Defects in Hybrid Halide Perovskites. *ACS Energy Lett.* **2017**, *2*, 2713–2714.

(48) Jung, Y.-K.; Calbo, J.; Park, J.-S.; Kim, S.; Whalley, L.; Walsh, A. Luminescence of Polybromide Defects in Cs4PbBr6. *ChemRxiv* **2019**, DOI: 10.26434/chemrxiv.7629467.v2.

(49) Tasker, P.; Stoneham, A. An Appraisal of the Molecular Model for the Vk Centre. *J. Phys. Chem. Solids* **1977**, *38*, 1185–1189.

(50) Park, J.-S.; Yang, J.-H.; Barnes, T.; Wei, S.-H. Effect of Intermixing at CdS/CdTe Interface on Defect Properties. *Appl. Phys. Lett.* **2016**, *109*, 042105.

(51) Polyakov, A. Y.; Smirnov, N. B.; Shchemerov, I. V.; Saranin, D. S.; Le, T. S.; Didenko, S. I.; Kuznetsov, D. V.; Agresti, A.; Pescetelli, S.; Matteocci, F.; Di Carlo, A. . Trap States in Multication Mesoscopic Perovskite Solar Cells: A Deep Levels Transient Spectroscopy Investigation. *Appl. Phys. Lett.* **2018**, *113*, 263501.

(52) Correa-Baena, J.-P. et al. Homogenized Halides and Alkali Cation Segregation in Alloyed Organic-Inorganic Perovskites. *Science* **2019**, *363*, 627–631.

(53) Zohar, A.; Levine, I.; Gupta, S.; Davidson, O.; Azulay, D.; Millo, O.; Balberg, I.; Hodes, G.; Cahen, D. What Is the Mechanism of MAPbI3 P-Doping by I2? Insights From Optoelectronic Properties. *ACS Energy Lett.* **2017**, *2*, 2408–2414.

(54) Perdew, J. P.; Ruzsinszky, A.; Csonka, G. I.; Vydrov, O. A.; Scuseria, G. E.; Constantin, L. A.; Zhou, X.; Burke, K. Restoring the Density-Gradient Expansion for Exchange in Solids and Surfaces. *Phys. Rev. Lett.* **2008**, *100*, 136406.

(55) Blöchl, P. E. Projector Augmented-Wave Method. *Phys. Rev. B* **1994**, *50*, 17953.

(56) Kresse, G.; Furthmüller, J. Efficient Iterative Schemes for Ab Initio Total-Energy Calculations Using a Plane-Wave Basis Set. *Phys. Rev. B* **1996**, *54*, 11169.

(57) Heyd, J.; Scuseria, G. E.; Ernzerhof, M. Hybrid Functionals Based on a Screened Coulomb Potential. *J. Chem. Phys.* **2003**, *118*, 8207–8215.

(58) Meggiolaro, D.; De Angelis, F. First-Principles Modeling of Defects in Lead-Halide Perovskites: Best Practices and Open Issues. *ACS Energy Lett.* **2018**, *3*, 2206–2222.

(59) Cossi, M.; Barone, V.; Cammi, R.; Tomasi, J. Ab Initio Study of Solvated Molecules: A New Implementation of the Polarizable Continuum Model. *Chem. Phys. Lett.* **1996**, *255*, 327–335.

(60) Mennucci, B.; Tomasi, J. Continuum Solvation Models: A New Approach to the Problem of Solutes Charge Distribution and Cavity Boundaries. *J. Chem. Phys.* **1997**, *106*, 5151–5158.

(61) Frost, J. M. Calculating Polaron Mobility in Halide Perovskites. *Phys. Rev. B* **2017**, *96*, 195202.

(62) Frisch, M. J. et al. Gaussian16 Revision A.03. 2016; Gaussian Inc. Wallingford CT.

(63) Krukau, A. V.; Vydrov, O. A.; Izmaylov, A. F.; Scuseria, G. E. Influence of the Exchange Screening Parameter on the Performance of Screened Hybrid Functionals. *J. Chem. Phys.* **2006**, *125*, 224106.

(64) Stevens, W. J.; Krauss, M.; Basch, H.; Jasien, P. G. Relativistic Compact Effective Potentials and Efficient, Shared-Exponent Basis Sets for the Third-, Fourth-, and Fifth-Row Atoms. *Can. J. Chem.* **1992**, *70*, 612–630.

Supporting Information for "Accumulation of deep traps at grain boundaries in halide perovskites"

Ji-Sang Park,[*,†] Joaquín Calbo,[†] Young-Kwang Jung,[‡] Lucy Whalley,[†] and Aron Walsh[*,†,‡]

[†]Department of Materials, Imperial College London, Exhibition Road, London SW7 2AZ,UK
[‡]Department of Materials Science and Engineering, Yonsei University, Seoul 03722, Korea

E-mail: ji-sang.park@imperial.ac.uk; a.walsh@imperial.ac.uk

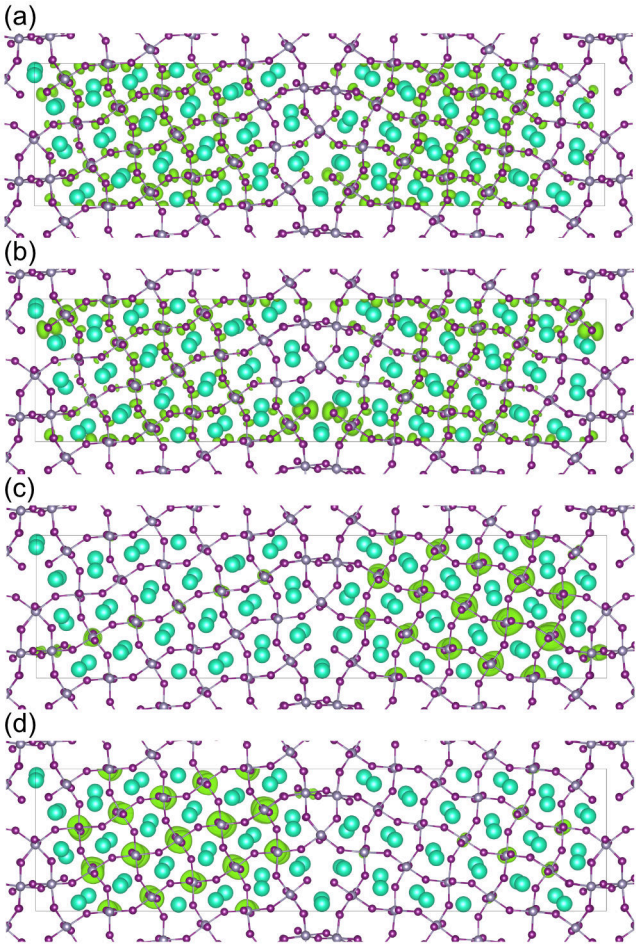

Figure S1. The charge density of eigenstates near the band edges at the Γ point. (b) and (c) is the highest occupied and the lowest unoccupied state, respectively. There is no state between (b) and (c). The eigenvalue of the (a) is lower than (b) by 0.03 eV. The eigenvalue of (c) and (d) is higher than that of (b) by 1.56 eV. The band gap of the corresponding bulk is 1.61 eV, which is only 0.06 eV higher than the band gap in the grain boundary calculation. The contour level is set to 10^{-4} bohr^{-3}. The atomic structures are drawn using the visualization for electronics and structural analysis (VESTA) package.[1]

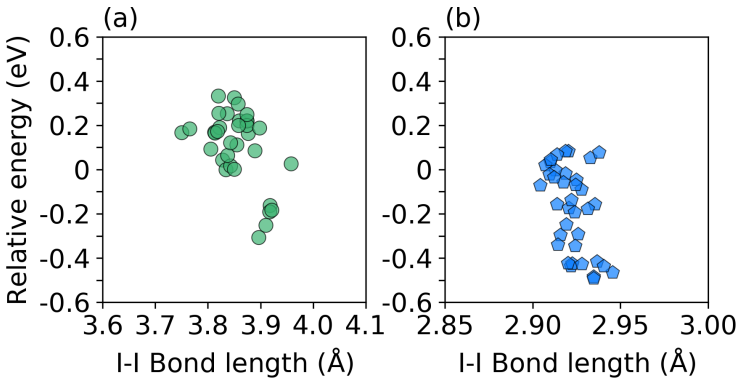

Figure S2. (a) The relative total energy of negatively charged iodine interstitial (I_i^-) as a function of the I-I bond length. (b) The relative total energy of positively charged iodine interstitial (I_i^{1+}) as a function of the I-I bond length. The total energy of the defects in the bulk region is set to 0 eV. The total energy generally decreases as the bond length increases.

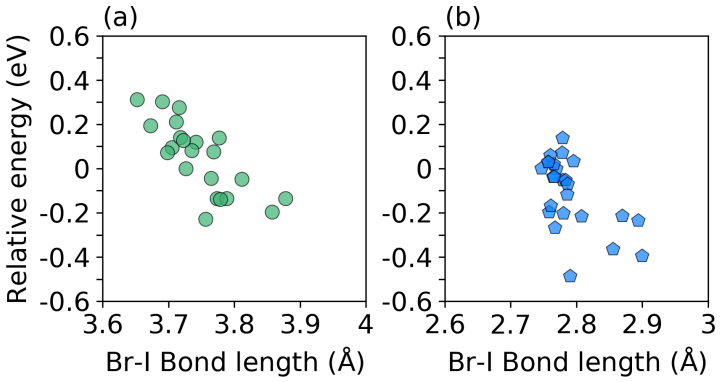

Figure S3. The relative total energy of bromine interstitial in (a) negatively (Br_i^{1-}) and (b) positively charged state (Br_i^{1+}) as a function of the Br-I bond length. There is a negative correlation between the relative total energy and bond length.

(1) Momma, K.; Izumi, F. VESTA 3 for three-dimensional visualization of crystal, volumetric and morphology data. *J. Appl. Crystallogr.* **2011**, 44, 1272-1276.